ELSEVIER

Contents lists available at ScienceDirect

# Journal of Alloys and Compounds

journal homepage: www.elsevier.com/locate/jalcom





# Facile fabrication of Mn-N doped porous carbon nanocages with enhanced oxygen reduction reaction activity

Kang Hu<sup>a,1</sup>, Xufen Xiao<sup>b,1</sup>, Peng Du<sup>c</sup>, Haibin Yang<sup>a</sup>, Zhihao Shen<sup>a</sup>, Guobiao Jin<sup>a</sup>, Fengzhi Wang<sup>d</sup>, Feng Pan<sup>a</sup>, Qinghe Zhao<sup>a,\*</sup>, Zirui Lou<sup>a,\*</sup>

- <sup>a</sup> School of Advanced Materials, Peking University Shenzhen Graduate School, Shenzhen 518055, Guangdong, PR China
- b Centre for Advanced Structural Materials, City University of Hong Kong Shenzhen Research Institute, Greater Bay Joint Division, Shenyang National Laboratory for Materials Science, Shenzhen 518057, PR China
- <sup>c</sup> Integrated Analysis and Testing Centre, Liaoning Academy of Materials, Shenyang 110167, Liaoning, PR China
- d State Key Laboratory of Silicon and Advanced Semiconductor Materials, School of Materials Science and Engineering, Zhejiang University, Hangzhou 310027, PR China

#### ARTICLE INFO

#### Keywords: ORR Mn-based Catalysts Electrocatalyst Mn-N<sub>5</sub> moiety

#### ABSTRACT

Mn-based oxygen reduction reaction (ORR) catalysts have high expectations, but cost and stability have always been the key problems to be solved in their industrialization. Herein, a novel electrocatalyst consisted of  $Mn-N_x$  doping sites within carbon frameworks was fabricated through a simple thermal and pickling treatment. The catalyst showed well-defined nanocage structure and excellent ORR performance with a half-wave potential of 0.85 V and a current density of 6 mA cm<sup>-2</sup> – these values are comparable to most Mn-based catalysts and commercial Pt/C. The unique advantages of the catalyst are facile procedure, low cost and good stability. The activities of the possible active sites in Mn-NPC (N doped porous carbon) were compared using theoretical calculations and recent experimental evidence, and the results showed that Mn-N<sub>5</sub> moiety has lower free energy barrier and higher oxygen adsorption performance than Mn-N<sub>4</sub> and Mn-N<sub>3</sub> moieties to accelerate the ORR kinetics, which is of great significance for the subsequent design and directional synthesis of Mn-based catalysts.

### 1. Introduction

Carbon material dotted with transition metals as the ORR catalyst under alkaline electrolyte has been extensively studied on account of its extraordinary advantages over Pt-based catalysts, such as low price, excellent catalytic performance and strong quantum effect, etc [1,2]. In many reports, in terms of the activity in both alkaline and acid media, Fe-based and Co-based carbon catalysts are superior to Mn-based carbon catalysts [3]. However, it is mentioned that Fe-based and Co-based catalysts show less satisfactory durability in fuel cell and metal zinc-air battery applications [4]. The hydrogen peroxide (a by-product in the two-electron reaction pathway) produced during the parasitic reaction will cause the dissociation of active metal components via the Fenton reaction, which will seriously weaken the activity and life cycle of the catalyst [5,6].

The first solution to improve the durability of Fe/Co based catalysts is to introduce other transition metals [7]. The second solution is to

choose Mn instead of Fe or Co. Compared to the reaction of Fe and Co with hydrogen peroxide, the reaction between Mn and hydrogen peroxide is much less active, which will promote the stability of the electrocatalyst and make Mn-based catalyst more promising for applications in fuel cells [8,9].

At present, substantial researches focus on the transition metal and heteroatoms (N, P, S, etc) co-doped carbon materials [10–12]. Comparatively speaking, the heteroatom N is still considered to be the most widely applicable and most effective dopant [13]. On the one hand, N atom doping can provide active structural defects. On the other hand, nitrogen atoms have the role of anchoring active metal atoms into the carbon matrix [14]. Thus, transition metal and nitrogen co-doped catalysts are widely regarded as the most promising alternatives to Pt/C.

In principle, in order to further optimize the activity of ORR, the influence of the morphology of carbon nanomaterials should also be taken into consideration. Usually, the discrete nano-carbons tend to aggregate/restack when they are made into electrodes, causing low

E-mail addresses: zhaoqh@pku.edu.cn (Q. Zhao), zrlou@pku.edu.cn (Z. Lou).

<sup>\*</sup> Corresponding authors.

 $<sup>^{1}\,</sup>$  K. Hu and X. Xiao contributed equally to this work.

porosity and inferior mass/ion transport kinetics [15,16]. The unique three-dimensional interconnected porous network of carbon nanocages has a faster mass/charge transfer rate than the two-dimensional carbon nanomaterials [17] and the abundant defects on the outer surface are conducive to electron transfer and can provide more active sites [18]. Therefore, carbon nanocages usually exhibit higher electrochemical activity and durability during catalytic reactions [19].

Herein, we designed a type of Mn, N dual-doped porous carbon (Mn-NPC) nanocages through a one-step pyrolysis of sodium citrate, urea and manganese acetate. The carbon nanocages possess large specific surface areas, numerous micro-meso pores and rich active sites, which endows an excellent catalytic activity under alkaline condition for ORR. In addition, strong long-term stability and low cost are the unique advantages of this catalyst. Finally, Theoretical calculation and experimental results have shown that the Mn-N $_5$  structure has a stronger ORR activity compared to the Mn-N $_3$ /Mn-N $_4$  structures.

#### 2. Experimental

#### 2.1. Catalyst synthesis

Typically, 5.0 g of sodium citrate was thoroughly ground together with 0.5 g of urea and 50 mg of manganese acetate. Then, the resulting powder was calcined at 800 °C with a heating rate of 5 °C min $^{-1}$  under Ar. After pickling with 1 M HCl and washing with deionized (DI) water and ethanol, the as-obtained solid was dried in an 80 °C oven overnight. The sample obtained was denoted as Mn-NPC. The sample without addition of manganese acetate was also prepared and denoted as NPC. The chemicals used in this study were all purchased from Sigma-Aldrich and used without further purification.

#### 2.2. Material characterizations

X-ray diffraction (XRD) measurements of as-prepared samples were carried out at room temperature using a Bruker (D2 Phaser) diffractometer with Cu K $\alpha$  source ( $\lambda=1.5406$  Å) at a scanning rate of  $5^{\circ}$  min $^{-1}$ . X-ray photoelectron spectra (XPS) measurements were performed in a scanning X-ray microprobe (VG ESCALAB 220i-XL) with Al K $\alpha$  x-rays. The scanning electron microscopy (SEM) images were obtained on a field emission microscope (Philips XL-30). TEM and HRTEM images were obtained by using a JEOL JEM-2100 F high-resolution transmission electron microscope with an accelerating voltage of 200 kV. The elemental distribution and HAADF-STEM imaging were carried out by an X-ray energy dispersive spectroscopy (EDXS) system and a scanning transmission electron microscopy (STEM) unit (Hitachi HD 2700 C), respectively. Raman spectra were recorded using a Renishaw 2000 microscope. The  $N_2$  adsorption/desorption isotherms and pore structure parameters were obtained on a Quantachrome Analyzer (Nova 1200e).

#### 2.3. Electrochemical measurements

Electrochemical measurements were carried out in a standard three-electrode system on a CHI 660E electrochemical working platform (CH Instruments, Inc., Shanghai) under 1 M KOH electrolyte. A carbon rod electrode and a saturated calomel electrode were used as counter electrode and reference electrode, respectively. All the potentials measured were converted into the potential vs reversible hydrogen electrode (RHE).

The preparation procedure for electrochemical testing is the same as previous reports [2]. Specifically, 5 mg of catalyst was ultrasonically dispersed in a mixed solution containing 20  $\mu L$  of naphthol solution (5 wt%) and 480  $\mu L$  of isopropanol. Approximately 12  $\mu L$  of the above mixed solution was evenly dispersed on the glassy carbon surface in two portions, so that the catalyst loading was  $\sim 0.6$  mg cm $^{-2}$ . The loading of the benchmark catalyst Pt/C was controlled at  $\sim 0.25$  mg cm $^{-2}$ .

Cyclic voltammograms (CVs) were recorded under static-electrode

condition in 0.1 M KOH solution saturated with  $O_2$  or Ar at a scanning rate of 50 mV s<sup>-1</sup>. Linear sweep voltammetry (LSV) was conducted in 0.1 M  $O_2$ -saturated KOH solution by the rotating disk electrode (RDE) technique at a scanning rate of 10 mV s<sup>-1</sup>. RRDE experiment was conducted in 0.1 M  $O_2$ -saturated KOH solution at 1600 rpm. The durability of the catalyst was investigated by chronoamperometry (i-t) technique at 0.3 V. The methanol resistance of the catalyst was analyzed by observing the curve shift in the present of 3 M methanol in the electrolyte. The hydrogen peroxide yield and the number of transferred electrons can be calculated by the following two equations [2]:

$$H_2O_2(\%) = \frac{200I_r/N}{I_r/N + I_d}$$

$$n = \frac{4I_d}{I_r/N + I_d}$$

In which  $I_r$  and  $I_d$  are ring and disk current; the current collection efficiency of the Pt ring (N) is 0.38.

#### 2.4. Computational details

All calculations were carried out by spin-polarized DFT with the Vienna Ab initio Simulation Package (VASP) [20]. Electron exchange-correlation was expressed by the Perdew-Burke-Ernzerhof (PBE) functional within the generalized gradient approximation (GGA) [21]. To describe the ionic cores, the projector augmented wave (PAW) pseudopotential was applied [22]. The Monkhorst-Pack K-points were set to be  $3\times3\times1$  during geometry optimization. The plane wave energy cutoff, and convergence criterion for electronic energy and forces were set as 500 eV,  $10^{-5}$  eV, and 0.02 eV/Å, respectively. The van der Waals (vdW) interactions were taken into consideration by using the Grimme method (DFT-D3). The calculated lattice parameters are  $14.81\times14.81\times20$  Å in this work.

To calculate the change in Gibbs free energy ( $\Delta G$ ), the computational hydrogen electrode (CHE) model was employed [23,24]. The free energies (G) of each state were determined using the following expression [25]:

$$G = E + ZPE + \int C_P dT - TS + G_{pH}$$

where T is temperature and E is electronic energy. ZPE,  $\int C_P dT$ , and TS are the zero point energy, enthalpy change from 0 to T K contributed by molecular vibration, and entropy correction, which are obtained based on vibration analysis at 298.15 K.  $G_{\rm pH}$  is the free energy correction of pH, which can be calculated by  $G_{\rm pH} = k_B T \ln 10 \times {\rm pH}$ . In this work, the pH value was set as 14. The equilibrium potential of ORR is 0.401 V. The limiting potential ( $U_{\rm L}$ ) is the applied potential that makes every elementary step exergonic in the assumed mechanism.  $U_{\rm L}$  can be obtained by the equation of  $U_{\rm L} = \Delta G_{\rm MAX}/e$ .

# 3. Results and discussion

The preparation of carbon nanocages is based on the previous method for preparing 3D framework carbon. During the preparation process, Mn and N sources are introduced into the synthesis process [26, 27]. Compared to traditional pyrolysis of MOF materials [28] or polymers [29], this method has the advantage of a simpler synthesis process. Fig. 1a showed the fabrication process of Mn-NPC materials. During the preparation, the generated sodium carbonate could be act as the catalyst and the hard template to form the nanocage structure. A mixture of carbon dots and sodium carbonate was obtained when the calcination temperature was not high enough (400 °C $\sim$ 500 °C), while sodium carbonate was easily decomposed and the output of carbonization product was greatly reduced when the calcination temperature was set too high (over 900 °C) [27]. Thus, the calcination temperature here was set to

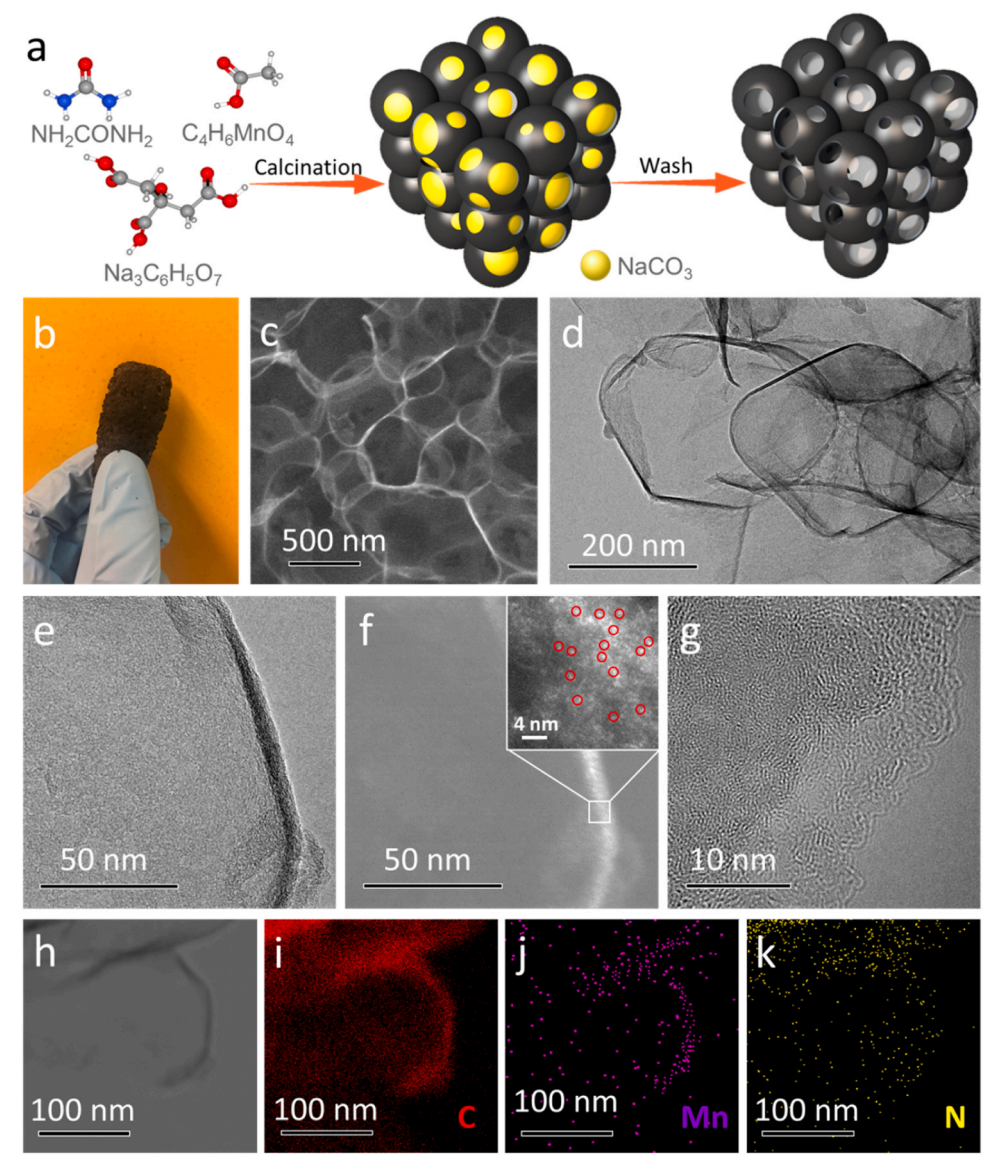


Fig. 1. (a) Synthesis scheme, (b) digital photo, (c) SEM image, (d,e) TEM images and (f) HAADF-STEM image, (g) HRTEM image, and (h-k) element mapping of Mn-NPC.

 $800\,^{\circ}\text{C},$  which promoted the formation of ultra-thin nanocage structures on the surface of sodium carbonate. Besides, N from urea and Mn from manganese acetate were decorated in the structural framework of carbon nanocages during the calcination process. Finally, a pickling step was required to remove sodium carbonate from the carbonization product.

The digital photo of fresh carbonization product was shown as Fig. 1b. It can be seen that the material we obtained is a kind of fluffy and foam-like carbon material. As revealed by the SEM image in Fig. 1c, ultra-thin, smooth and curved cage-like carbon nanomaterials were obtained, which cross-linked and integrated to form a three-dimensional foam-like network. No residues of sodium carbonate particles and Mn-related aggregate-particles on the surface of the material proved that they were eliminated after the pickling step and Mn mainly exists in the form of single atoms or small clusters. TEM images (Fig. 1d-e and Fig. S1) also proved its cage-like morphology and clean surface (without particles remaining). Such a nanocage structure could not only expose more active sites, but also greatly shorten the charge transfer pathway [30]. The bright areas in the HAADF-STEM image (Fig. 1f) were attributed to the presence of Mn component. It could be found that Mn was uniformly dispersed in the carbon nanocages. This may be due to

the high density of defects in carbon nanostructures, which allows manganese ions and nitrogen atoms to easily form chemical bonds with carbon atoms. HRTEM image (Fig. 1g) at the edge of carbon nanocages showed a partially graphitized carbon structure. The element mapping (Fig. 1h-k) obtained by EDS showed that C, N and Mn were uniformly distributed throughout the selected area of the nanocage, in accordance with the results of HAADF-STEM image.

Structure and composition information of as-obtained samples were investigated by XRD, Raman, nitrogen adsorption/desorption and XPS. The peaks corresponding to the (002) and (101) characteristic crystal planes of graphitic carbon were observed at  $26^{\circ}$  and  $44^{\circ}$  in the XRD patterns of Mn-NPC and NPC samples (Fig. 2a). The absence of peaks related to Mn suggests that the relevant particles were removed during the pickling step and partial Mn might be present in the amorphous Mn-Nx coordination, which is difficult to detect by XRD.

The Raman spectra of Mn-NPC and NPC samples (Fig. 2b) showed clearly visible D and G peaks at 1337 and 1590 cm $^{-1}$ , respectively. The G band was attributed to the bond stretching of all sp $^2$ -bonded pairs, while the D band arises from the sp $^3$  defect sites [31]. It is worth noting that the peak intensity ratio of D band to G band ( $\rm I_D/\rm I_G$ ) for Mn-NPC was larger than that of NPC, and the profile of D band for Mn-NPC was also

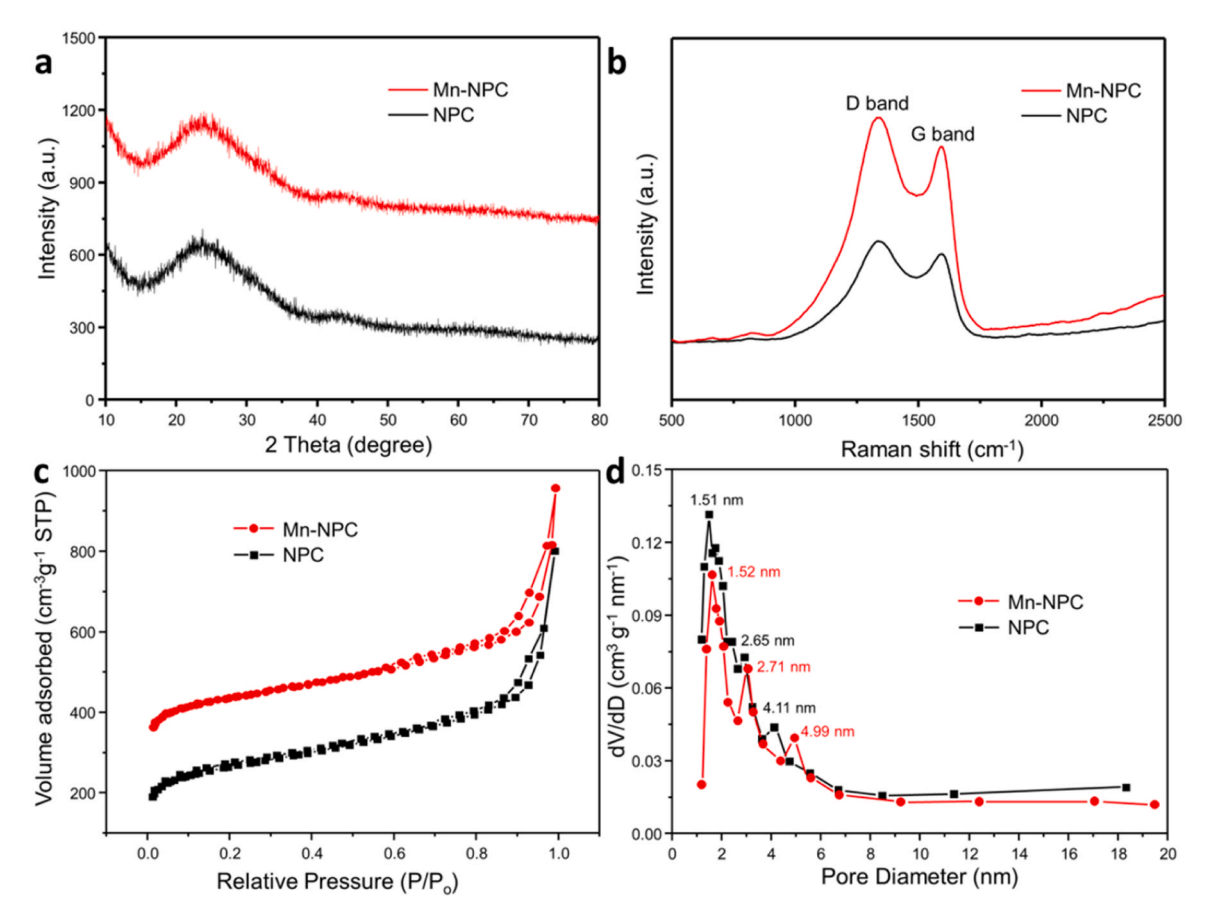


Fig. 2. (a) XRD patterns, (b) Raman spectra, (c) nitrogen adsorption/desorption isotherms and (d) pore size distribution of Mn-NPC and NPC.

broader than that of NPC, proving that higher level of defects formed after Mn doping [32,33].

The isotherm curves of Mn-NPC and NPC in Fig. 2c exhibit characteristics of Type I and Type IV, indicating that they may have both micropore and mesopore structures [34]. The data in the pore size distribution (Fig. 2d) confirmed their micro-meso hierarchical porous structure. Both Mn-NPC and NPC exhibit pores centered from 1.50 to 5.00 nm. Additionally, the specific surface area and total pore volume of Mn-NPC are 382.37 m² g $^{-1}$  and 0.56 cm³ g $^{-1}$ , respectively, which is larger than that of NPC (340.77 m² g $^{-1}$  and 0.48 cm³ g $^{-1}$ ), likely due to the additional defects induced by Mn doping. The increased specific surface area provides more accessible active sites and electrochemical

surfaces for the electrolyte, which is highly beneficial for the oxygen reduction reaction (ORR).

The X-ray photoelectron spectroscopy (XPS) survey spectra presented in Fig. 3a reveal the presence of carbon (C), nitrogen (N), and oxygen (O) elements in both Mn-NPC and NPC samples. The signal of Mn in Mn-NPC is not clearly visible in the full spectrum due to the low amount of Mn added during the preparation process. However, the high-resolution XPS spectrum of Mn (inset in Fig. 3a) show two obvious peaks at 641.8 and 653.5 eV, accompanied by a satellite peak at 646.2 eV, which were characteristics of divalent Mn, indicating the presence of Mn in Mn-NPC [35,36]. The surface element content of Mn-NPC and NPC was listed in Table S1 (Supplementary Information), which shows

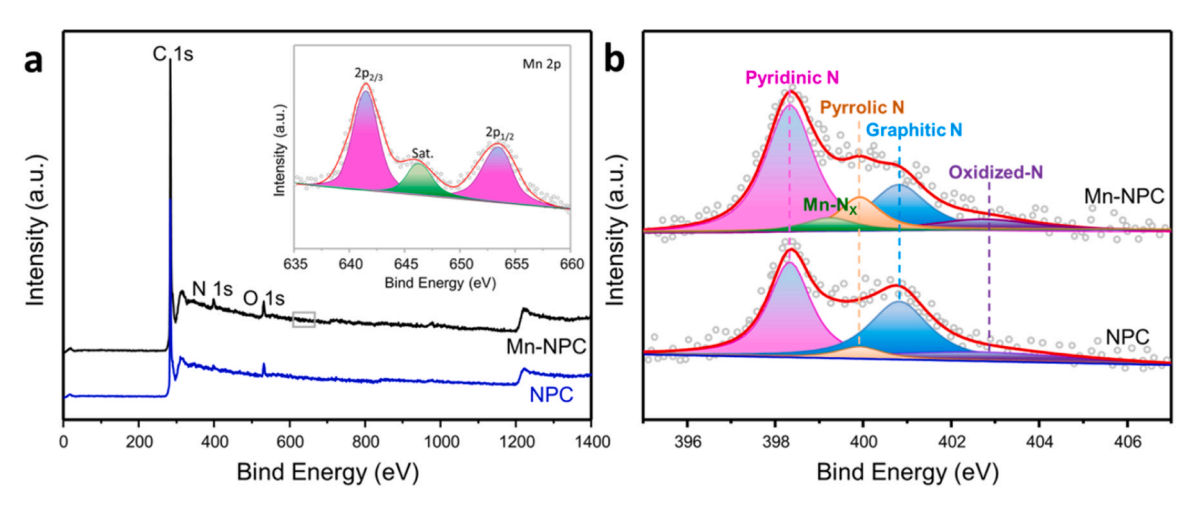


Fig. 3. (a) XPS survey spectra of Mn-NPC and NPC, and Mn 2p XPS spectrum for Mn-NPC (inset); (b) The high resolution N 1 s XPS spectrum of Mn-NPC and NPC.

5.93 at% of N and 0.14 at% of Mn on the surface of Mn-NPC, while only 4.14 at% of N on the surface of NPC, indicated that the introduction of Mn can significantly enhance N doping in the carbon matrix.

In order to analyze the existence form of N species, corresponding high-resolution XPS spectra was collected and analyzed. As shown in Fig. 3b, the N 1 s spectra of Mn-NPC can be divided into five peaks at 398.3, 399.2, 399.9, 400.8 and 402.8 eV, corresponding to pyridinic-N, Mn-N $_{\rm x}$ , pyrrolic-N, graphitic-N and oxidized-N, respectively [8]. In addition to Mn-N $_{\rm x}$  species, pyridinic-N and graphitic-N were also generally considered as the active component [31]. Specifically, pyridinic-N can promote the transfer of electrons and reduce the overpotential of ORR, while graphitic-N can improve the electrocatalytic activity in terms of limiting current density [37,38]. According to statistics as shown in Table S1 and Fig. S2, the total contents and

proportion of active components in Mn-NPC is higher than that of NPC.

The C 1 s spectrum for Mn-NPC (Fig. S3) can be deconvoluted into three component peaks centered at 284.6, 285.4, and 286.5 eV, corresponding to C=C (sp<sup>2</sup>-centers), C=N/C-O and C=O/C-N, respectively [39]. The presence of the latter two peaks confirms that the N and O atoms were successfully incorporated into the carbon framework.

The O 1 s spectrum for Mn-NPC (Fig. S4) can be deconvoluted into three peaks centered at 531.5, 532.5 and 533.6 eV. The peak at 531.5 eV can be assigned to the carboxyl group (COO—) and the oxygen double bond to carbon (O=C-O) [40]. The peak at 532.5 eV is related to the adsorbed water on the hydrophilic surface, and its presence ensures that the catalyst surface can be more accessible to the electrolyte in the electrochemical reaction [41]. The appearance of these oxygen groups is attributed to adsorption from the air (moisture, O<sub>2</sub>, or CO<sub>2</sub>) and the

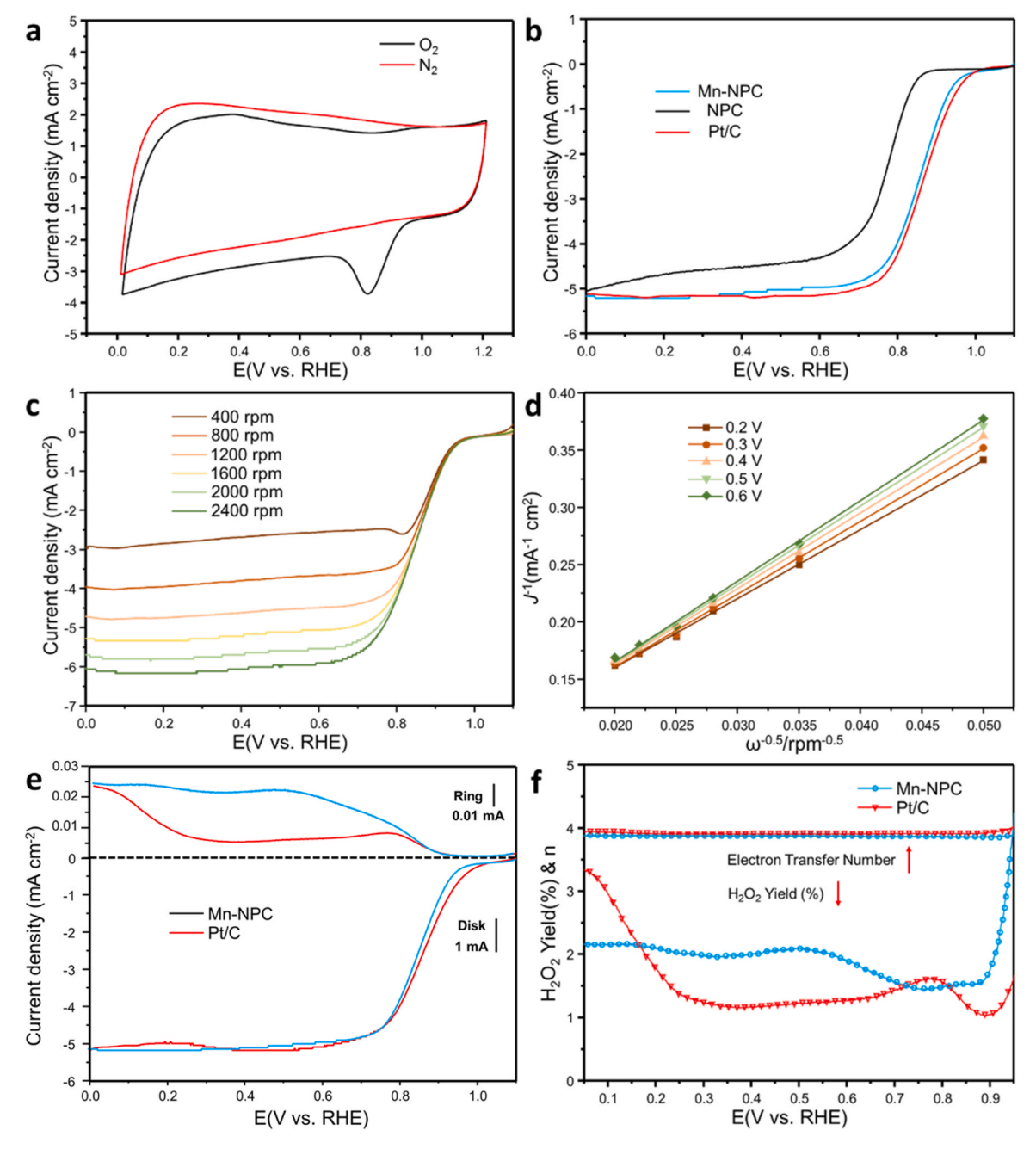


Fig. 4. (a) Cyclic voltammetry (CV) curves of Mn-NPC; (b) Linear scan voltammetry (LSV) curves of Mn-NPC, NPC, and Pt/C; (c) Linear scan voltammetry (LSV) curves of Mn-NPC at various rotation speeds; (d) K-L plots of the Mn-NPC; (e) RDE and RRDE voltammograms of Mn-NPC and Pt/C; (f) Variation of electron transfer number (n) and  $H_2O_2$  yield (%) with the disk electrode potential at Mn-NPC and Pt/C catalysts.

oxygen-containing components in the original carbon source (sodium citrate). Oxygen doping disrupts the electrical neutrality of the  $\rm sp^2$  carbon lattice and promotes the ORR reaction [38,40].

The onset potential and half-wave potential are two main performance indexes used to measure ORR catalysts. Fig. 4a exhibits the cyclic voltammetric (CV) curves of Mn-NPC measured in 0.1 M KOH electrolyte, showing a clear cathodic peak at 0.82 V in the oxygen-saturated electrolyte, but not in the nitrogen-saturated electrolyte. To further determine the ORR performance of the catalyst, the polarization curves of Mn-NPC, NPC, and 20 wt% commercial Pt/C were recorded at a rotation speed of 1600 rpm as shown in Fig. 4b. The onset potential of Mn-NPC is as high as 0.95 V, very close to that of Pt/C. The half-wave potential of Mn-NPC is 0.85 V, only 10 mV less than that of 20 wt% commercial Pt/C. Under alkaline conditions, the performance of Mn-NPC is comparable to that of Pt/C and Mn-based carbon material catalysts. At less than 0.8 V, the diffusion-limiting current showed a very stable trend with a well-defined plateau, which implied that the catalytic reaction on Mn-NPC was an efficient four-electron reaction pathway [42].

RDE (Rotating Disk Electrodes) and RRDE (Rotating Ring-Disk Electrodes) are commonly used in ORR electrochemical testing due to their ability to improve mass transfer speed and ensure dynamic stability of oxygen concentration on the electrode surface. We obtained RDE curves for Mn-NPC at different rotation rates (Fig. 4c) and calculated corresponding kinetic parameters using the Koutecky-Levich (K-L) equation based on the above data (Fig. 4d). The well-defined linear relationship of the K-L plots illustrates the first-order reaction kinetics towards dissolved O2. The numbers of electron transfers at various potentials (0.2–0.6 V) in the reaction calculated based on the slopes of the K-L plots were close to 4, confirming that Mn-NPC catalyst demonstrated a strong preference for the four-electron reaction pathway. The RRDE test further confirmed the results obtained from the RDE curves, with a stable range of electron transfers over Mn-NPC for potentials ranging from 0.05 to 0.95 V (Fig. 4e-f). This indicates a smooth and electrochemically stable reaction process over Mn-NPC [43]. The yield of hydrogen peroxide over Mn-NPC is also lower than other types of catalysts in this range of potentials (Table S2), suggesting that the two-electron reaction pathway in the ORR reaction was suppressed while the high selectivity of the four-electron reaction route was revealed.

In addition to catalyst activity, the stability and methanol resistance of ORR catalyst are also important performance indicators. The stability of the catalyst was evaluated by observing the degree of current decay of the i–t chronoamperometric plot (Fig. S5) of Mn-NPC. The current decay of Mn-NPC is only 7% after 50,000 s, lower than that of commercial Pt/C (13% current decay) and most other reported Mn-based catalysts (Table S2). Observation of the polarization curves before and after the injection of 3 M methanol into 0.1 M KOH (Fig. S6) reveals a negligible curve shift, indicating the low sensitivity of Mn-NPC to methanol.

The cost of catalyst is a crucial factor for its commercial application. Our cost estimation reveal that the raw material cost of Mn-NPC is a mere  $50~\text{US}\$\,\text{kg}^{-1}$  (details see Table S3), which is only 1% of commercial Pt/C catalysts. Moreover, Mn-NPC is significantly cheaper than other manganese-based catalysts (Table S4), making it more cost-effective for industrial use. This significant cost difference is primarily due to the nitrogen source of Mn-NPC, which is derived from inexpensive chemicals like urea and sodium citrate. In contrast, other literature reports the carbon or nitrogen source as being derived from costly chemicals such as carbon nanotubes [44], graphene oxide [45], ZIF-8 [46,47], etc.

The outstanding performance of Mn-NPC can be attributed to several factors. Firstly, the nanocage structure combined with the hierarchical porous characteristics facilitates electron transfer, mass transport, and electrolyte penetration. Secondly, the active sites located at the marginal area of the carbon nanocage are more likely to come into contact with the electrolyte, thereby increasing their exposure and accessibility. Finally, the incorporation of Mn enhances the content and proportion of

active nitrogen species, particularly Mn-N<sub>x</sub> species.

The three-dimensional interconnected porous network of carbon nanocages and abundant defects will facilitate the formation of M-N<sub>5</sub> (M = Fe, Co, Ni, Mn) structures [48]. Compared to M-N<sub>3</sub>/M-N<sub>4</sub> plane structures, M-N<sub>5</sub> can induce the breaking of electron density symmetry, which is more conducive to the adsorption and activation of oxygen, so as to improve the activity of the catalyst [28]. In order to verify our hypothesis and explain the effect of atomic coordination environment on the ORR properties of the catalyst, we simulated the ORR processes of Mn-N<sub>3</sub>/N<sub>4</sub>/N<sub>5</sub> under alkaline conditions by density functional theory (DFT). The optimized structures of Mn-N<sub>3</sub>, Mn-N<sub>4</sub>, and Mn-N<sub>5</sub> are depicted in Fig. 5a, 5b, and 5c. Fig. 5d illustrates the ORR free energy profiles on these sites. Along the ORR pathway, the potential-limiting step on all three sites is  $OH^* + e^- \rightarrow * + OH^-$ , with limiting potentials of 0.88, 0.46, and 0.25 V at U=0~V vs. RHE. This indicates that increasing the coordination number of nitrogen atoms enhances the ORR activity of the single Mn center. Furthermore, the relationship between free energy and adsorption strength of the significant intermediate OH\* in step (4) was investigated to explain the essential factor influencing ORR activity (Fig. 5e). The results indicate that increasing the coordination number of nitrogen atoms around the single Mn center weakens the adsorption energy of OH, leading to a lower limiting potential for the step of  $OH^* + e^- \rightarrow * + OH^-$ . Based on these calculations, it is concluded that the five-coordinated Mn-N5 moiety can more effectively promote the ORR than configurations with a lower coordination number under alkaline conditions. Moreover, recent research [28] has reported the synthesis of an atomically dispersed Mn-N5 catalyst with outstanding performance by precisely axial coordination of pyridinic-N into two-dimensional porous nanocarbon sheets, providing experimental evidence for the above theoretical calculations.

The four-electron reduction of  $O_2$  of ORR in alkaline media involves the following four steps [49,50]:

$$O_2(g) + H_2O(l) + e^- + * \rightarrow OOH^* + OH^-$$
 (1)

$$OOH^* + e^- \rightarrow O^* + OH^-$$
 (2)

$$O^* + H_2O(l) + e^- \to OH^* + OH^-$$
 (3)

$$OH^* + e^- \rightarrow ^* + OH^- \tag{4}$$

#### 4. Conclusions

In summary, we have developed an efficient and cost-effective strategy for fabricating electrocatalysts with desirable nanocage structures, hierarchical pore characteristics and Mn-N doping. The resulting Mn-NPC catalyst exhibits good catalytic activity, with an onset potential  $(E_{onset})$  of 0.95 V and a half-wave potential  $(E_{1/2})$  of 0.85 V, which is comparable to that of commercial Pt/C and other Mn-based catalysts under alkaline solution conditions. The long-term stability (7% current decay after 50,000 s) and low cost make Mn-NPC a promising alternative among Mn-based catalysts. Theoretical calculations and experimental results suggested that the Mn-N5 coordination in the carbon framework is more beneficial for ORR than Mn-N3 and Mn-N4 coordinations, raising expectations for the precise regulation of coordination environments for ORR development. In conclusion, we have developed a manganese-based catalyst Mn-NPC that offers simple synthesis process, low cost and excellent stability simultaneously, providing a new approach for the commercialization of non-noble metal ORR catalysts.

#### CRediT authorship contribution statement

Kang Hu: Investigation, Writing – original draft. Xufen Xiao: Investigation, Writing – original draft. Peng Du: Conceptualization,

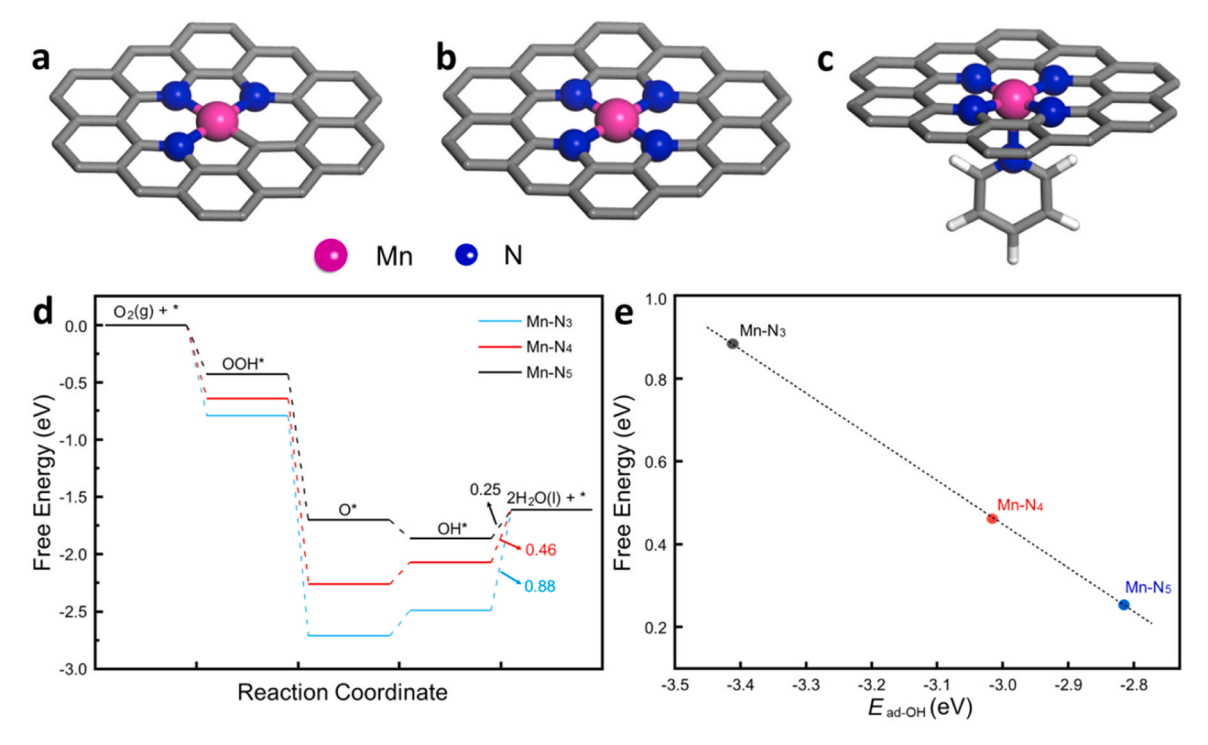


Fig. 5. Optimized structures of (a) Mn-N<sub>3</sub>, (b) Mn-N<sub>4</sub>, and (c) Mn-N<sub>5</sub>; (d) Free energy profiles of ORR on Mn-N<sub>x</sub> sites; (e) Scaling relationship between  $\Delta G_{MAX}$  and adsorption energies of OH.

Resources, Investigation. Haibin Yang: Investigation. Zhihao Shen: Writing – review & editing. Guobiao Jin: Investigation. Fengzhi Wang: Resources, Investigation. Feng Pan: Supervision, Funding acquisition. Qinghe Zhao: Conceptualization, Supervision, Funding acquisition. Zirui Lou: Conceptualization, Writing – review & editing, Supervision.

# **Declaration of Competing Interest**

The authors declare that they have no known competing financial interests or personal relationships that could have appeared to influence the work reported in this paper.

# **Data Availability**

No data was used for the research described in the article.

# Acknowledgments

The authors would like to acknowledge the financial support from the Shenzhen Science and Technology Research Grant (No. JCYJ20200109140416788), the Shenzhen Fundamental Research Program (No. GXWD20201231165807007—20200807111854001), the Natural Science Foundation of Shenzhen (JCYJ20190813110605381) and the National Natural Science Foundation of China (52102201).

# Appendix A. Supporting information

Supplementary data associated with this article can be found in the online version at doi:10.1016/j.jallcom.2023.171819.

#### References

- [1] N. Xu, Y. Zhang, T. Zhang, Y. Liu, J. Qiao, Nano Energy 57 (2019) 176-185.
- [2] P. Du, F.X. Ma, F. Lyu, K. He, Z. Li, J. Lu, Y.Y. Li, Chem. Commun. 55 (2019) 5789–5792.
- [3] X. Xiong, Y. Li, Y. Jia, Y. Meng, K. Sun, L. Zheng, G. Zhang, Y. Li, X. Sun, Nanoscale 11 (2019) 15900–15906.

- [4] D. Banham, S. Ye, K. Pei, J. Ozaki, T. Kishimoto, Y. Imashiro, J. Power Sources 285 (2015) 334–348.
- [5] C. Walling, Acc. Chem. Res. 8 (1975) 125-131.
- [6] F.D. Coms, ECS Trans. 16 (2008) 235–255.
- [7] H.G. Li, S.L. Di, P. Niu, S.L. Wang, J. Wang, L. Li, Energy Environ. Sci. 15 (2022) 1601–1610
- [8] J. Li, M. Chen, D.A. Cullen, S. Hwang, M. Wang, B. Li, K. Liu, S. Karakalos, M. Lucero, H. Zhang, Nat. Catal. 1 (2018) 935–945.
- [9] Y. Zhong, X. Liang, Z. He, W. Tan, J. Zhu, P. Yuan, R. Zhu, H. He, Appl. Catal. B-Environ. 150 (2014) 612–618.
- [10] J. Masa, W. Xia, M. Muhler, W. Schuhmann, Angew. Chem. Int. Ed. 54 (2015) 10102–10120.
- [11] Z.W. Chen, D. Higgins, A.P. Yu, L. Zhang, J.J. Zhang, Energy Environ. Sci. 4 (2011) 3167–3192.
- [12] X. Ma, C. Chang, Y. Zhang, P. Niu, X. Liu, S. Wang, L. Li, ACS Sustain. Chem. Eng. 8 (2020) 8318–8383.
- [13] S.C. Cai, Z.H. Meng, H.L. Tang, Y. Wang, P. Tsiakaras, Appl. Catal. B-Environ. 217 (2017) 477–484.
- [14] H. Kim, K. Lee, S.I. Woo, Y. Jung, Phys. Chem. Chem. Phys. 13 (2011) 17505–17510.
- [15] X. Zhang, Y. Zhu, A.M. Bruck, L.M. Housel, L. Wang, C.D. Quilty, K.J. Takeuchi, E. S. Takeuchi, A.C. Marschilok, G. Yu, Energy Storage Mater. 19 (2019) 439–445.
- [16] Z. Lyu, D. Xu, L. Yang, R. Che, R. Feng, J. Zhao, Y. Li, Q. Wu, X. Wang, Z. Hu, Nano Energy 12 (2015) 657–665.
- [17] H. Wang, X. Liu, P. Niu, S. Wang, L. Li, Matter 2. 6 (2020) 1377–1413.
- [18] B. Fang, J.H. Kim, M. Kim, M. Kim, J.S. Yu, Phys. Chem. Chem. Phys. 11 (2009) 1380–1387.
- [19] H. Fan, K. Mao, M. Liu, O. Zhuo, J. Zhao, T. Sun, Y. Jiang, X. Du, X. Zhang, Q. Wu, R. Che, L. Yang, Q. Wu, X. Wang, Z. Hu, J. Mater. Chem. A 6 (2018) 21313–21319.
- [20] G. Kresse, J. Furthmüller, Phys. Rev. B 54 (1996) 11169.
- [21] J.P. Perdew, K. Burke, M. Ernzerhof, Phys. Rev. Lett. 77 (1996) 3865-3868
- [22] G. Kresse, D. Joubert, Phys. Rev. B 59 (1999) 1758-1775.
- [23] J.K. Nørskov, J. Rossmeisl, A. Logadottir, L. Lindqvist, J.R. Kitchin, T. Bligaard, H. Jonsson, J. Phys. Chem. B 108 (2004) 17886–17892.
- [24] C. Guo, T. Zhang, X. Deng, X. Liang, W. Guo, X. Lu, C.-M.L. Wu, ChemSusChem 12 (2019) 5126–5132.
- [25] W. Cheng, P. Yuan, Z. Lv, Y. Guo, Y. Qiao, X. Xue, X. Liu, W. Bai, K. Wang, Q. Xu, J. Zhang, Appl. Catal. B-Environ. 260 (2020), 118198.
- [26] D. Li, X. Ren, Q. Ai, Q. Sun, L. Zhu, Y. Liu, Z. Liang, R. Peng, P. Si, J. Lou, J. Feng, Adv. Energy Mater. 8 (2018) 1802386.
- [27] B. Yang, J. Chen, S. Lei, R. Guo, H. Li, S. Shi, X. Yan, Adv. Energy Mater. 8 (2018) 1702409.
- [28] Y. Qin, C.Z. Guo, Z.H. Ou, C.L. Xu, J. Energy Chem. 80 (2023) 542–552.
- [29] X.F. Zhu, R. Amal, X.Y. Lu, Small 15 (2019) 1804524.
- [30] Y. Tang, R. Liu, S. Liu, B. Zheng, Y. Lu, R. Fu, D. Wu, M. Zhang, M. Rong, Carbon 141 (2019) 704–711.
- [31] L. Liu, G. Zeng, J. Chen, L. Bi, L. Dai, Z. Wen, Nano Energy 49 (2018) 393-402.

- [32] A. Sadezky, H. Muckenhuber, H. Grothe, R. Niessner, U. Pöschl, Carbon 43 (2005) 1731–1742.
- [33] G. Compagnini, O. Puglisi, G. Foti, Carbon 35 (1997) 1793–1797.
- [34] J.R. Matos, L.P. Mercuri, A.M. Kruk, M. Jaroniec, Langmuir 18 (2002) 884-890.
- [35] Y. Wang, X. Ding, F. Wang, J. Li, S. Song, H. Zhang, Chem. Sci. 7 (2016) 4284-4290.
- [36] Y. Sun, X. Hu, W. Luo, F. Xia, Y. Huang, Adv. Funct. Mater. 23 (2013) 2436–2444.
- [37] C. Tang, H.F. Wang, X. Chen, B.Q. Li, T.Z. Hou, B. Zhang, Q. Zhang, M.M. Titirici, F. Wei, Adv. Mater. 28 (2016) 6845-6851.
- [38] C. Tang, B. Wang, H.-F. Wang, Q. Zhang, Adv. Mater. 29 (2017) 1703185.[39] L.Z. Fan, S. Qiao, W. Song, M. Wu, X. He, X. Qu, Electrochim. Acta 105 (2013) 299-304.
- [40] Z. Liu, Z. Zhao, Y. Wang, S. Dou, D. Yan, D. Liu, Z. Xia, S. Wang, Adv. Mater. 29 (2017) 1606207.

- [41] H. Wu, J. Geng, H. Ge, Z. Guo, Y. Wang, G. Zheng, Adv. Energy Mater. 6 (2016) 1600794.
- [42] A. Bonakdarpour, M. Lefevre, R. Yang, F. Jaouen, T. Dahn, J.P. Dodelet, J.R. Dahn, Electrochem. Solid St. 11 (2008) B105.
- [43] J. Liang, Y. Jiao, M. Jaroniec, S.Z. Qiao, Angew. Chem. Int. Ed. 51 (2012) 11496-11500.
- [44] X. Guo, S. Xue, X. Zhang, et al., J. Alloy. Compd. 953 (2023), 169992.
- [45] L. Bai, Z.Y. Duan, et al., Appl. Catal. B: Environ. 257 (2019), 117930.
- [46] J.J. Huo, X.J. Cao, Y.P. Tian, et al., Nanoscale 15 (2023) 5448-5457.
- [47] L. Gong, J.W. Zhu, F.J. Xia, et al., ACS Catal. 13 (2023) 4012-4020.
- [48] Q. Wu, L. Yang, X. Wang, Z. Hu, Sci. China Chem. 63 (2020) 665-681.
- [49] X. Guo, S. Lin, J. Gu, S. Zhang, Z. Chen, S. Huang, ACS Catal. 9 (2019) 11042-11054.
- [50] Q. Lv, W. Si, J. He, L. Sun, C. Zhang, N. Wang, Z. Yang, X. Li, X. Wang, W. Deng, Y. Long, C. Huang, Y. Li, Nat. Commun. 9 (2018) 3376.